MODELLING OF WING - BODY COMBINATIONS IN UNSTEADY SUPERSONIC FLOW

L.H. van Zyl
AEROTEK, CSIR
Pretoria, South Africa

Abstract

The method of images for modelling wing–body interference, commonly used in steady and unsteady subsonic flow, was evaluated as a possible solution to the problem of modelling wing–body interference in unsteady supersonic flow. It was implemented in a panel method in which lifting surfaces are represented by acceleration potential doublet panels and bodies by axial doublet lines. The major advantages of axial singularity methods compared to surface panel methods are fewer unknowns, simpler integrals and freedom from internally reflected shock waves. Surface panel methods, on the other hand, are naturally suited to wing–body interference problems. The method of images combined with an axial singularity method allows the modelling of wing–body interference while retaining the advantages of the axial singularity method. The method was evaluated by considering how well the boundary condition is satisfied over the body surface in cases with strong wing–body interference, convergence of results with respect to panelling and by comparison with experimental data. The results indicate that the method can readily be applied to practical configurations.

Nomenclature

B	$\sqrt{M^2-1}$
D_{rs}	velocity influence coefficient
e	semi–span of lifting surface element
I_0	$\int_{s_1}^{s_2} \frac{\exp(-\omega_r s)}{(r^2+s^2)^{1/2}}\,ds$, integral relating acceleration and velocity potential
K_1, K_2	kernel functions $r\frac{\partial I_0}{\partial r}$ and $r^3\frac{\partial}{\partial r}(\frac{1}{r}\frac{\partial I_0}{\partial r})$
M	free stream Mach number
q	local acceleration potential doublet strength, normalized by $U^2/2$
Q	singularity strength, defined in equation (1)
r	$\sqrt{y^2+z^2}$
R	$\sqrt{x^2-B^2r^2}$
s_1	$(x-MR)/B^2$
s_2	$(x+MR)/B^2$
T_1, T_2	direction cosine functions
U	free stream velocity
x,y,z	$x_0-\xi$, $y_0-\eta$, $z_0-\zeta$
x_0,y_0,z_0	coordinates of receiving point in a sending panel coordinate system
x_s	reference x–coordinate of sending panel
ϕ	perturbation velocity potential, normalized by U
ω	angular frequency
ω_r	wave number $i\omega/U$
ξ,η,ζ	coordinates of sending point in a sending panel coordinate system

Introduction

The calculation of unsteady air loads on aircraft is an essential step in flutter clearance, active control and gust load alleviation work. The doublet lattice method [1] provides this capability for lifting surfaces in subsonic flow. The method has been extended to include bodies and wing–body combinations by means of slender body theory [2] to model the flow around isolated bodies and either a method of interference panels on the body surface [3] or the method of images [4] to model wing–body interference. The constant pressure lifting surface method combined with a body surface panel method for subsonic flow [5] is a higher order method providing this capability. The lifting surface problem in supersonic flow has been solved successfully and several computer codes are available which are capable of calculating unsteady air loads on interfering lifting surfaces. The modelling of wing–body interference in unsteady supersonic flow proves to be more difficult and few fully developed solutions are available [6].

The present method is distinguished by the following :

- it uses the acceleration potential formulation
- lifting surfaces are modelled by piecewise constant pressure distributions

- bodies are modelled by piecewise linear axial doublet distributions
- the method of images is used to model wing–body interference

The main advantages of such a scheme are simplicity, commonality with subsonic methods and versatility. A previous paper [7] on this method dealt with the basic theory and the method of images in supersonic flow – this paper addresses the modelling of lifting surfaces and bodies as single elements in more detail.

Lifting surfaces

To solve a flow problem in general it is necessary to find a solution for the velocity and other fluid properties which satisfies the governing differential equations as well as the boundary conditions. Analytical solutions to the complete differential equations exist only for the simplest of problems. The panel or finite element method is a powerful tool for finding approximate solutions to complex problems for which analytical solutions do not exist. The principle is to model the flow by means of a finite number of singularities, each of which satisfies the governing differential equation. The strengths of the singularities are determined from a set of linear equations so that the boundary conditions are satisfied at a number of collocation points equal to the number of singularities. The major part of the numerical work is devoted to the calculation of the matrix of influence coefficients. Element i,j of the matrix can be regarded as the velocity that singularity j would induce at collocation point i if it had unit strength.

The acceleration potential doublet is a convenient singularity to use in unsteady flow because there exists a simple relationship between the doublet strength and load on lifting surfaces, and the integration needed to calculate induced velocities and pressures is limited to the physical panel, i.e. excluding the wake. The expressions for the influence coefficients can be simplified by assuming that the doublet strength varies harmonically with ξ.

$$q(\xi,\eta) = Q \exp(-\omega_r(\xi - x_s)) \tag{1}$$

With this doublet strength distribution, the expression for the velocity potential induced by an acceleration potential doublet panel of unit strength ($Q = 1$) is

$$\phi = \frac{\exp(-\omega_r(x_0 - x_s))}{8\pi} \int_{-e}^{+e} \int_{a+b\eta}^{c+d\eta} \frac{x_0}{r} \frac{\partial I_0}{\partial r} \, d\xi \, d\eta \tag{2}$$

where $\xi = a+b\eta$ and $\xi = c+d\eta$ define the panel leading and trailing edges, respectively. This expression is applicable if all of the sending panel lies within the forward Mach cone of the receiving point. In the case of a lifting surface panel being cut by the Mach cone, the induced potential is expressed as an integral from the leading edge to the Mach cone, minus an integral from the trailing edge to the Mach cone.

$$\phi = \frac{\exp(-\omega_r(x_0 - x_s))}{8\pi} \left\{ \int_{\eta_1}^{\eta_2} \int_{a+b\eta}^{x_0 - Br} \frac{x_0}{r} \frac{\partial I_0}{\partial r} \, d\xi \, d\eta - \int_{\eta_3}^{\eta_4} \int_{c+d\eta}^{x_0 - Br} \frac{x_0}{r} \frac{\partial I_0}{\partial r} \, d\xi \, d\eta \right\} \tag{3}$$

The spanwise integration limits can be either an edge of the panel or the intersection of the forward Mach cone of the receiving point with the leading or trailing edge of the sending panel. The expression for the influence coefficient is found by differentiating the applicable expression for ϕ with respect to the normal of the receiving element. Cunningham [8] showed that this order of operation was necessary to avoid a non–integrable singularity on the Mach cone. The case of a sending panel lying entirely within the forward Mach cone of a receiving point poses no special problems. In the case of the sending element being cut by the Mach cone, the influence coefficient is given by (only the first term of equation (3) is shown)

$$D_{rs} = \frac{\exp(-\omega_r(x_0 - x_s))}{8\pi} \left\{ \int_{\eta_1}^{\eta_2} \frac{T_1}{r^2} \int_{Br}^{x_B} K_1(x,r) \, dx \, d\eta + \int_{\eta_1}^{\eta_2} \frac{T_2}{r^4} \left[\int_{Br}^{x_B} K_2(x,r) \, dx - Br \, K_1(Br,r) \right] d\eta \right\} \tag{4}$$

where $x_B = x_0 - (a+b\eta)$. Both K_1 and K_2 are singular at the lower limit of chordwise integration. The singularity of K_1 is integrable but not the singularity of K_2. The singularity of K_1 in the integrand of the second spanwise integral cancels the chordwise integrated singularity of K_2 at $x = Br$. At spanwise integration limits defined by the intersection of the Mach cone with the leading edge, x_B goes to Br and the integrand of the second spanwise integral goes to infinity. To resolve this singularity, K_1 is divided into a part K_1' which is zero at $x = Br$ and a part K_1'' which is singular at $x = Br$. (These expressions correspond to those given in reference 9.)

$$K_1'(x,r,M,\omega_r) = -\int_{s_1}^{s_2} \frac{r^2 \exp(-\omega_r s)}{(r^2+s^2)^{3/2}} \, ds \tag{5}$$

$$K_1''(z,r,M,\omega_r) = -\frac{Mr^2}{R}\left[\frac{\exp(-\omega_r s_2)}{(r^2+s_2{}^2)^{1/2}} + \frac{\exp(-\omega_r s_1)}{(r^2+s_1{}^2)^{1/2}}\right] \tag{6}$$

$K_1''(x_B,r)$ is added to the integrand of the second spanwise integral and the spanwise integral of $K_1''(x_B,r)$ subtracted separately.

$$D_{rs} = \frac{\exp(-\omega_r(x_0-x_s))}{8\pi}\left\{\int_{\eta_1}^{\eta_2}\frac{T_1}{r^2}\int_{Br}^{x_B} K_1(z,r)\,dx\,d\eta + \int_{\eta_1}^{\eta_2}\frac{T_2}{r^4}\left[\int_{Br}^{x_B} K_2(x,r)\,dx + Br\,K_1''(x_B,r) - Br\,K_1''(Br,r)\right]d\eta - \int_{\eta_1}^{\eta_2}\frac{T_2}{r^4}Br\,K_1''(x_B,r)\,d\eta\right\} \tag{7}$$

The term $Br\,K_1''(x_B,r) - Br\,K_1''(Br,r)$ can be expressed as

$$Br\,K_1''(x_B,r) - Br\,K_1''(Br,r) = \int_{Br}^{x_B} Br\frac{\partial K_1''}{\partial x}\,dx \tag{8}$$

This yields an expression for D_{rs} in which the chordwise integrals have, after a change of integration variable to R, completely regular integrands.

$$dx = \frac{dR}{(\frac{\partial R}{\partial x})} = \frac{dR}{(\frac{x}{R})} = \frac{R}{x}\,dR \tag{9}$$

$$D_{rs} = \frac{\exp(-\omega_r(x_0-x_s))}{8\pi}\left\{\int_{\eta_1}^{\eta_2}\frac{T_1}{r^2}\int_0^{R_B}\frac{R}{x}K_1(x(R),r)\,dR\,d\eta + \int_{\eta_1}^{\eta_2}\frac{T_2}{r^4}\int_0^{R_B}\frac{R}{x}\left[K_2(x(R),r) + Br\frac{\partial K_1''}{\partial x}(x(R),r)\right]dR\,d\eta - \int_{\eta_1}^{\eta_2}\frac{T_2}{r^4}Br\,K_1''(x_B,r)\,d\eta\right\} \tag{10}$$

where $R_B = \sqrt{x_B{}^2 - B^2r^2}$. The first two spanwise integrals can be solved by normal quadrature or curve fitting followed by analytical integration as is done in the subsonic doublet lattice method [10]. The last spanwise integral can be written as

$$\int_{\eta_1}^{\eta_2}\frac{T_2\,B\,\frac{R_B}{r^2}\,K_1''(x_B,r)}{R_B\,r}\,d\eta \tag{11}$$

where the numerator is a regular function. The problem with evaluating this integral is that r can become small at $\eta = y_0$ if z_0 is small, and R_B can become zero at the end points of the integration interval. In cases of interest these two conditions do not occur at the same value of η, therefore the integration interval can be divided so that different techniques can be used depending on which one of r and R_B is smaller. Where r is smaller, a polynomial approximation is made to r times the integrand and the resulting integral of a polynomial divided by r is solved analytically. The analytical integration is simplified by changing the integration variable to y.

$$\int_{\eta_1}^{\eta_2}\frac{T_2\,B\,\frac{1}{r^2}\,K_1''(x_B,r)}{r}\,d\eta \approx \int_{y_1}^{y_2}\frac{b_4y^4+b_3y^3+b_2y^2+b_1y+b_0}{\sqrt{y^2+z^2}}\,dy \tag{12}$$

where $y_1 = y_0-\eta_2$ and $y_2 = y_0-\eta_1$. Over those parts of the integration interval where R_B is smaller, the integral is cast in the form

$$\int_{\eta_1}^{\eta_2}\frac{f(\eta)}{R_B}\,d\eta \tag{13}$$

where $f(\eta) = T_2\,B\,R_B\,K_1''(x_B,r)/r^3$ is a regular function. The integration variable is changed to u, given by

$$u(\eta) = \int\frac{1}{R_B}\,d\eta \tag{14}$$

$$d\eta = \frac{du}{(\frac{du}{d\eta})} = \frac{du}{(\frac{1}{R_B})} = R_B\,du \tag{15}$$

The integral (13) can then be written as

$$\int_{\eta_1}^{\eta_2}\frac{f(\eta)}{R_B}\,d\eta = \int_{u(\eta_1)}^{u(\eta_2)} f(\eta(u))\,du \tag{16}$$

which can be evaluated using normal quadrature. R_B can readily be expressed as the square root of a quadratic in η.

$$R_B = \sqrt{a_2\eta^2+a_1\eta+a_0} \tag{17}$$

For a panel leading edge defined by $\xi = a+b\eta$, the coefficients are

$$\begin{aligned} a_2 &= b^2 - B^2 \\ a_1 &= -2b(x_0-a) + 2B^2y_0 \\ a_0 &= (x_0-a)^2 - B^2(y_0{}^2+z_0{}^2) \end{aligned} \tag{18}$$

The integral in (14) can be solved analytically with the result

$$u(\eta) = \frac{2\sqrt{a_1\eta+a_0}}{a_1} \qquad \text{if } a_2 = 0$$

$$u(\eta) = \frac{1}{\sqrt{a_2}}\ln\left|2\sqrt{a_2}\sqrt{a_2\eta^2+a_1\eta+a_0} + 2a_2\eta+a_1\right| \qquad \text{if } a_2 > 0$$

$$u(\eta) = \frac{-1}{\sqrt{-a_2}} \sin^{-1}\left(\frac{2a_2\eta+a_1}{\sqrt{a_1^2-4a_2a_0}}\right) \qquad \text{if } a_2 < 0 \tag{19}$$

The inverse relationship $\eta(u)$ is given by

$$\eta(u) = \frac{(\frac{a_1 u}{2})^2 - a_0}{a_1} \qquad \text{if } a_2 = 0$$

$$\eta(u) = \frac{4a_2a_0-(a_1+\exp(\sqrt{a_2}\,u))^2}{4a_2\exp(\sqrt{a_2}\,u)} \qquad \text{if } a_2 > 0 \text{ and } u < u_0$$

$$\eta(u) = \frac{(a_1-\exp(\sqrt{a_2}\,u))^2-4a_2a_0}{4a_2\exp(\sqrt{a_2}\,u)} \qquad \text{if } a > 0 \text{ and } u > u_0$$

$$\eta(u) = \frac{\sqrt{a_1^2-4a_2a_0}\,\sin(-\sqrt{-a_2}\,u) - a_1}{2a_2} \qquad \text{if } a_2 < 0 \tag{20}$$

where

$$u_0 = \frac{\ln\sqrt{a_1^2-4a_2a_0}}{\sqrt{a_2}} \tag{21}$$

With this formulation no improper integrals occur in the evaluation of the nonplanar influence coefficient. To achieve high accuracy, however, some aspects of the numerical evaluation demand special attention.

In near–coplanar cases the chordwise integration in equation (10) is performed over a wide range of R/r values. The integrand of the chordwise integral in the second term has a peculiar behavior at low values of R/r and $r\omega_r$ which necessitates the subdivision of the integration interval. Satisfactory results can be achieved with a linear subdivision in $\ln(R/r+1)$, which is shown in figure 1 together with the integrand at zero frequency. Each sub–interval is integrated using five–point Gauss quadrature. High accuracy is important because the error in the evaluation of this integral in near–coplanar cases is magnified by the factor $1/r^4$ in the spanwise integration.

At integration limits determined by the intersection of the leading edge with the forward Mach cone of the receiving point, the integrands of the first two spanwise integrals go to zero with infinite slope. Polynomials cannot approximate this behavior properly, but square root functions can. Curve fits using a second degree polynomial, a fourth degree polynomial and a fourth degree polynomial plus square root functions are shown in figure 2. It is clear that the square root terms drastically improve the accuracy of the curve fit. The effect on the accuracy of the method can be illustrated using the simple test case of a supersonic biplane with the upper wing lying within the two dimensional flow field of the lower wing (figure 3). With both wings at unit angle of attack, the loading on the upper wing should be zero, while the pressure differential in the centre of the lower wing should be equal to $4/B$ over the entire chord. Figure 4 shows the error in the pressure over the inboard strips of the upper and lower wings calculated with the different approximations at $M = \sqrt{2}$ and $k = 0$. The fact that the error on the upper wing is an approximate mirror image of the error on the lower wing indicates that the main source of error is the coplanar calculation of the pressure over the lower wing. The use of boxes with an aspect ratio of two in stead of one leads to a much increased error. From figure 3 it can be seen that, if an aspect ratio of one had been used, the portion of the leading edge which influences point 1 would span three elements. This would essentially amount to a subdivision of the integration interval. This is the case with the influence of the leading edge of the lower wing at a collocation point of the upper wing, as can be seen in figure 3, and explains why the error is attributed mainly to the calculation of the coplanar influence coefficients.

The high frequency behavior of the method is demonstrated using the popular test case of a rectangular wing with aspect ratio 2 pitching about mid chord at a reduced frequency of 1.5 and Mach No. of $\sqrt{2}$. The pressure distribution over the inboard strip is shown in figure 5. Rather than plotting a single point per box, the piecewise continuous pressure distribution according to equation (1) is shown. The exponential variation smooths the real part, but increases the discontinuities in the imaginary part. Although the assumed variation of the pressure distribution simplifies the calculation of influence coefficients, it is by no means necessary and can be changed easily. This case was also analysed with the sign of the exponent in equation (1) reversed as well as with a constant distribution (zero exponent in equation (1)). The results with the positive exponent is shown in figure 6. The imaginary part is smoothed, while the discontinuities in the real part are increased. The results with a constant distribution are shown in figure 7 and are compared to results obtained by Hounjet [11]. The agreement is satisfactory. The different pressure distributions would necessarily influence the convergence of the integrated results. The convergence histories for the unsteady lift and pitching moment are shown in figures 8 and 9, respectively. The results from the 10 by 10 and 20 by 20 grids were extrapolated to obtain an approximation to the fully converged result. The scaling

was chosen so that the axes span a 10% variation around this approximated converged result. Also shown is the convergence history of the ZONA51C program [12]. Both the values and the convergence behavior is in agreement.

Bodies

Whereas pressure distributions on lifting surfaces may be zero–order discontinuous in both directions, axial singularities must be zero–order continuous. This is achieved by using overlapping hat functions and letting the doublet strength go to zero at the body end points. The points on the surface which are used to define the body geometry and discretisation are projected to the axis along Mach lines. A typical element is illustrated in figure 10. The velocity potential induced by a body axial singularity is given by

$$\phi = Q \frac{\exp(-\omega_T(x_0-x_S))}{8\pi} \left\{ \int_{\xi_1}^{\xi_2} \frac{z_0}{r} \frac{\partial I_0}{\partial r} g_1(\xi)\, d\xi + \int_{\xi_2}^{\xi_3} \frac{z_0}{r} \frac{\partial I_0}{\partial r} g_2(\xi)\, d\xi \right\} \tag{22}$$

and the velocity influence coefficient by

$$\begin{aligned} D_{rs} = \frac{\exp(-\omega_T(x_0-x_S))}{8\pi} \Bigg\{ & \frac{1}{\xi_2-\xi_1} \Bigg[\frac{T_1}{r^2} \Bigg[(x_0-\xi_1) \int_{x_0-\xi_2}^{x_0-\xi_1} K_1(z,r)\, dx \\ & - \int_{x_0-\xi_2}^{x_0-\xi_1} x\, K_1(z,r)\, dx \Bigg] + \frac{T_2}{r^4} \Bigg[(x_0-\xi_1) \int_{x_0-\xi_2}^{x_0-\xi_1} K_2(z,r) \\ & + Br \frac{\partial K_1''}{\partial x}(z,r)\, dx - \int_{x_0-\xi_2}^{x_0-\xi_1} x \left(K_2(z,r) + Br \frac{\partial K_1''}{\partial x}(z,r) \right) \\ & + Br \frac{\partial K_1''}{\partial x}(z,r)\, dx \Bigg] \Bigg] + \frac{1}{\xi_3-\xi_2} \Bigg[\frac{T_1}{r^2} \Bigg[\int_{x_0-\xi_3}^{x_0-\xi_2} x\, K_1(z,r)\, dx \\ & - (x_0-\xi_3) \int_{x_0-\xi_3}^{x_0-\xi_2} K_1(z,r)\, dx \Bigg] + \frac{T_2}{r^4} \Bigg[\int_{x_0-\xi_3}^{x_0-\xi_2} x \left(K_2(z,r) \right. \\ & \left. + Br \frac{\partial K_1''}{\partial x}(z,r) \right) + Br \frac{\partial K_1''}{\partial x}(z,r)\, dx \\ & - (x_0-\xi_3) \int_{x_0-\xi_3}^{x_0-\xi_2} K_2(z,r) + Br \frac{\partial K_1''}{\partial x}(z,r)\, dx \Bigg] \Bigg] \Bigg\} \end{aligned} \tag{23}$$

For the numerical evaluation, the integration variable is changed to R as was done for lifting surface elements. In the case of an axial singularity being cut by the Mach cone (cases 2 and 3 in figure 10), no special treatment is required. The integration interval is simply truncated.

Although the method uses axial singularities, it is not equivalent to slender body theory. It is compared in figures 11 and 12 to the HPP method of Garcia–Fogeda and Liu [13] and slender body theory for the Saturn SA–1 launch vehicle pitching about its apex at $k = 1.8$. The agreement with the HPP results is good. In figure 13 the aerodynamic damping of the same rocket in first bending mode is compared to the HPP result. The agreement is good over the Mach number range 1.5 to 2.4. Above Mach 2.4, one of the segments becomes superinclined, which the present method does not model properly. Below Mach 1.5, the HPP method shows a sharp downward trend which is not reflected by the present method or the measured values.

Wing–body interference

Panel methods are limited in their applicability by the differential equation they assume. Apart from this inherent limitation, a panel method can be evaluated by the extent to which it satisfies the boundary condition, and by its convergence properties. The former is especially important for wing–body interference, since a single collocation point may be used to represent a complete body segment. The applicability of the method of images in supersonic flow has been demonstrated in some detail in reference 7, but one example is repeated here. The test case is that of the F5 wing with the AIM9 tip missile, which is shown in figure 14. A good panel method should satisfy the boundary condition to a high degree of accuracy using a very fine panelling scheme, while the integrated results should be insensitive to the panelling scheme. The fifth panelling scheme of the tip store shown in figure 14 was used to calculate residual normal velocities on the missile body for the whole wing at a steady angle of attack at Mach 1.35. The 9 sections through the missile body at which the residual normal velocities are shown are also indicated on figure 14. The results in figure 15 are scaled so that the component of the free stream normal to the plane of the wing would be represented by the radius of the body. It is clear that the boundary condition is satisfied to a very high degree, although the method of images does not cancel shocks properly.

To investigate the convergence properties of the present method, generalized forces were calculated for a pitching mode about the mid chord at the root and a plunging mode, using the five panelling schemes shown in figure 14. The plunge mode has unit amplitude and the amplitude of the pitch mode is chosen so that the amplitude of oscillation of the leading edge of the wing root is unity. The calculations were done for reduced frequencies of 0 to 0.75 in increments of 0.05 and Mach 1.35 The generalized forces are normalized with the wing area. The results are presented in figures 16 to 19 and show good convergence

from the second panelling scheme. The convergence results with only the panelling of the tip store being progressively refined would not mean much if the contribution of the tip store was negligible. The magnitude of the contribution of the tip store can be seen from the figures to be substantial, therefore the convergence results presented are significant.

Load distributions on the wing with under wing store were compared to NLR experimental results [14,15]. The geometry and discretization of the configuration is shown in figure 20. The calculated and measured load distributions on the wing at Mach 1.35 and reduced frequency 0.1 are shown in figures 21 to 24. The quasi–steady measured values are shown together with the real parts of the unsteady measured values. The experimental error in the quasi–steady measurements is expected to be less than the error in the unsteady measurements, while the unsteady effects should be small at this low reduced frequency. The real part of both the normal force and pitching moment is slightly overpredicted while the imaginary parts are underpredicted. This is in agreement with the results presented in [6]. The spanwise distributions of lift and pitching moment and effect of the store is in good agreement with the experimental results.

The unsteady side force on the store in various stages of completeness is compared to the measured values in figures 25 and 26. The values are in good agreement although the trend with Mach number seems to be reversed. This is also in agreement with [6].

Conclusions

A method for modelling wing–body combinations in unsteady supersonic flow has been developed which makes use of acceleration potential doublet panels for wings, axial doublet lines for bodies and the method of images for modelling wing–body interference. The method satisfies the boundary conditions to an acceptable degree over the entire surface of a body, even in the immediate vicinity of a lifting surface adjacent to the body. The convergence of calculated results with respect to panelling has been shown to be satisfactory, and a limited comparison with experimental results showed good agreement. The modelling similarity with the method of images for unsteady subsonic flow should improve continuity between subsonic and supersonic results where the method of images is used in the subsonic analysis.

The present study considered the use of the method of images with an axial doublet line representation of bodies. This representation limits the type of body that can be modelled to circular cross sections, but there is no reason why it could not be used to good effect with other axial singularity methods for bodies of non–circular cross section. It may also improve the convergence of surface panel methods.

References

[1] Albano, E. and Rodden, W.P., "A Doublet–Lattice Method for Calculating Lift Distributions on Oscillating Surfaces in Subsonic Flows", AIAA Journal, Vol. 7, No. 2, February 1969, pp. 279–285; also Errata AIAA Journal, Vol. 7, No. 11, November 1969, p. 2192.

[2] Miles, John W., "On Non–Steady Motion of Slender Bodies", The Aeronautical Quarterly, Vol. II, pp.183–194, November 1950.

[3] Giesing, J.P., Kalman, T.P. and Rodden, W.P., "Subsonic Steady and Unsteady Oscillatory Aerodynamics for Multiple Interfering Wings and Bodies", Journal of Aircraft, Vol. 9, No. 10, pp. 693–702, October 1972.

[4] Giesing, J.P., Kalman, T.P. and Rodden, W.P., "Subsonic Unsteady Aerodynamics for General Configurations, Part II", AFFDL–TR–71–5.

[5] Liu, D.D., Lee, H.W. and Chen, P.C.,"Unsteady Subsonic Aerodynamics for Bodies and Wings with External Stores Including Wake Effect", Paper 91–060, International Forum on Aeroelasticity and Structural Dynamics 1991.

[6] Chen, P.C. and Liu, D.D., "Unsteady Supersonic Computations of Arbitrary Wing–Body Configurations Including External Stores", J. Aircraft, Vol. 27, No. 2, February 1990, pp. 108–116.

[7] Van Zyl, L.H., "Modelling of Wing–Body Combinations in Unsteady Supersonic Flow", Proceedings of the International Forum on Aeroelasticity and Structural Dynamics 1993, Volume 1, pp. 189–204.

[8] Cunningham, A.M. Jr., "Oscillatory Supersonic Kernel Function Method for Interfering Surface", *Journal of Aircraft*, Vol. 11, No. 11, 1974, pp.664–670.

[9] Harder, R.L. and Rodden, W.P., "Kernel Function for Nonplanar Oscillating Surfaces in Supersonic Flow", J. Aircraft, Vol. 8, No. 8, August 1971, pp. 677–679.

[10] Rodden, W.P., Giesing, J.P. and Kalman, T.P., "Refinement of the Nonplanar Aspects of the Subsonic Doublet–Lattice Lifting Surface Method", Journal of Aircraft, Vol. 9, No. 1, pp. 69–73, January 1972.

[11] Hounjet, M.H.L., "Improved Potential Gradient Method to Calculate Airloads on Oscillating Supersonic Interfering Surfaces", J. Aircraft, Vol. 19, No. 5, May 1982, pp.390–399.

[12] Liu, D.D., James, D.K., Chen, P.C. and Pototzky, A.S., "Further Studies of Harmonic Gradient Method for Supersonic Aeroelastic Applications", J. Aircraft, Vol. 28, No. 9, 1991, pp. 598–605.

[13] Garcia–Fogeda, P. and Liu, D.D., "Analysis of Unsteady Aerodynamics for Elastic Bodies in Supersonic Flow", J. Aircraft, Vol. 24, No. 12, December 1987, pp. 833–840

[14] Tijdeman, J. et.al., "Transonic Wind–Tunnel Tests on an Oscillating Wing with External Stores; Parts I to IV", NLR–TR–78106, May 1979.

[15] Tijdeman, J. et.al., "Results of Transonic Wind–Tunnel Measurements on an Oscillating Wing with External Store (Data Report)", NLR–TR–78030 U, September 1978.

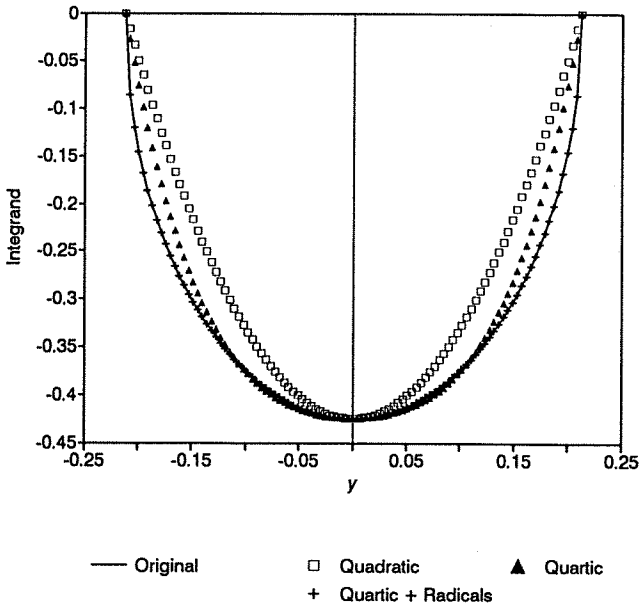

Figure 2 Approximations to coplanar spanwise integrand at zero frequency.

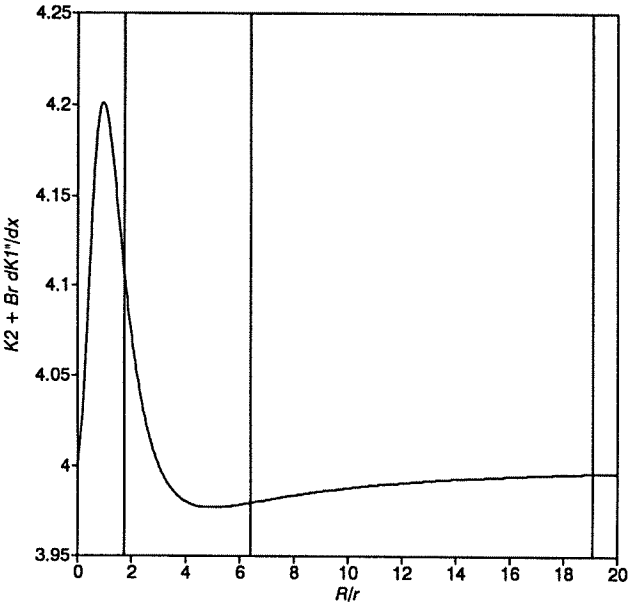

Figure 1 Nonplanar chordwise integrand at $M = \sqrt{2}$ and zero frequency.

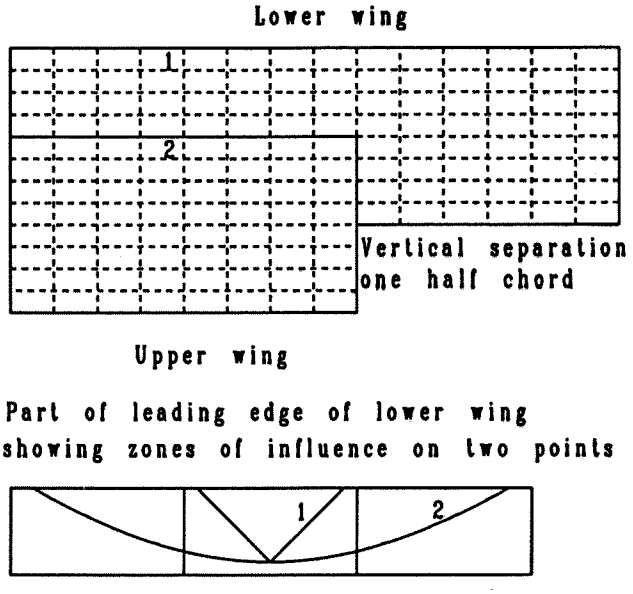

Figure 3 Geometry of supersonic biplane.

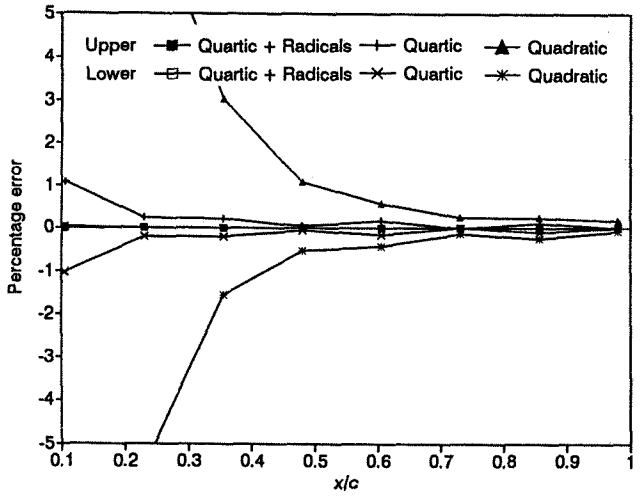

Figure 4 Error in solution of supersonic biplane with different approximations to spanwise integrand.

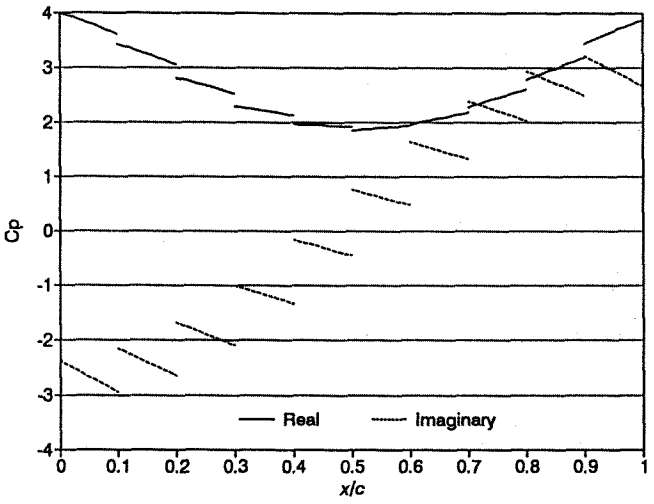

Figure 5 Chordwise distribution of pressure coefficient difference over inboard strip of rectangular wing using negative exponent in distribution function.

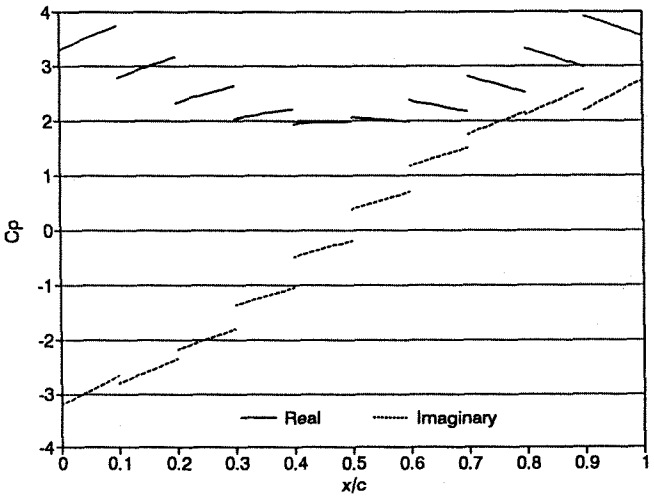

Figure 6 Chordwise distribution of pressure coefficient difference over inboard strip of rectangular wing using positive exponent in distribution function.

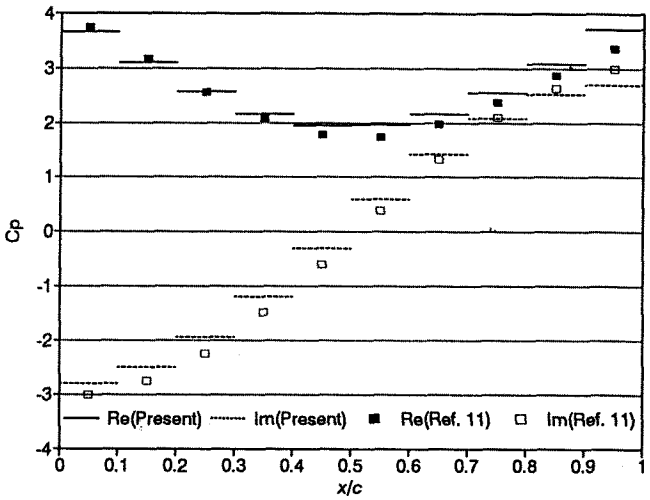

Figure 7 Chordwise distribution of pressure coefficient difference over inboard strip of rectangular wing using constant distribution function, compared to data from reference 11.

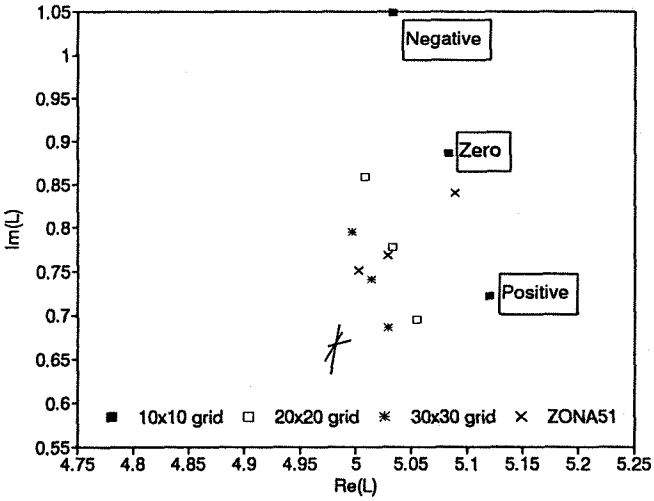

Figure 8 Convergence of lift of rectangular wing with different distribution functions, compared to ZONA51.

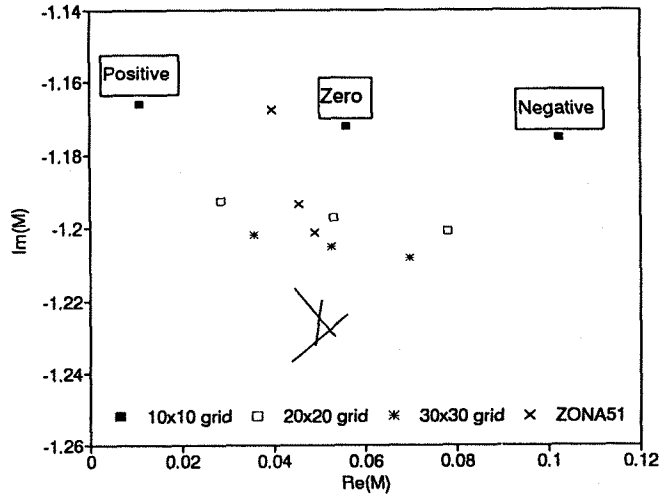

Figure 9 Convergence of pitching moment of rectangular wing with different distribution functions, compared to ZONA51.

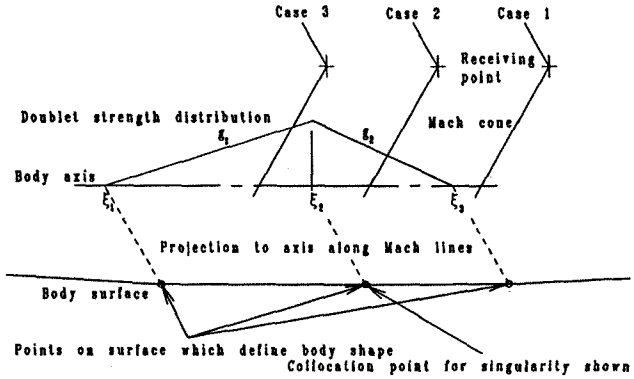

Figure 10 Construction of axial singularity from given points on body surface.

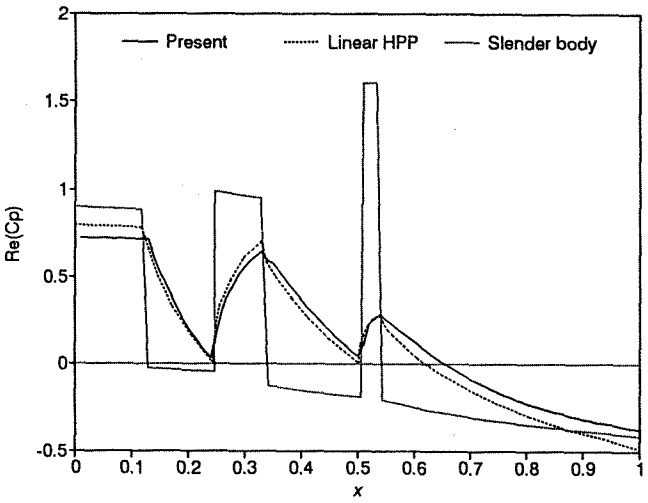

Figure 11 Real part of unsteady pressure on surface of Saturn SA–1 launch vehicle pitching about apex at $k = 1.8$ and $M = 2$.

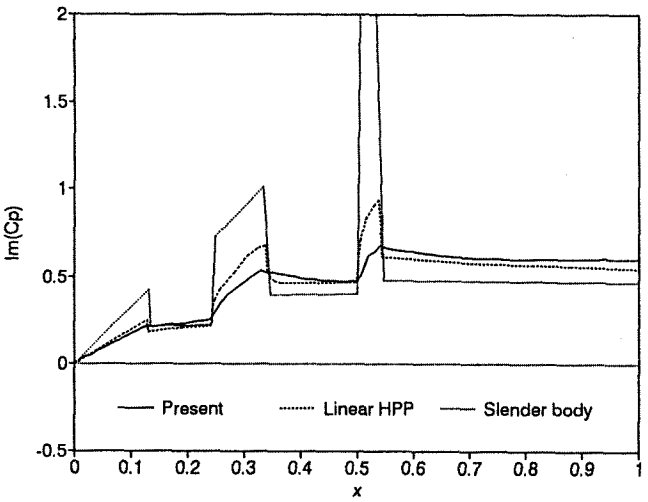

Figure 12 Imaginary part of unsteady pressure on surface of Saturn SA–1 launch vehicle pitching about apex at $k = 1.8$ and $M = 2$.

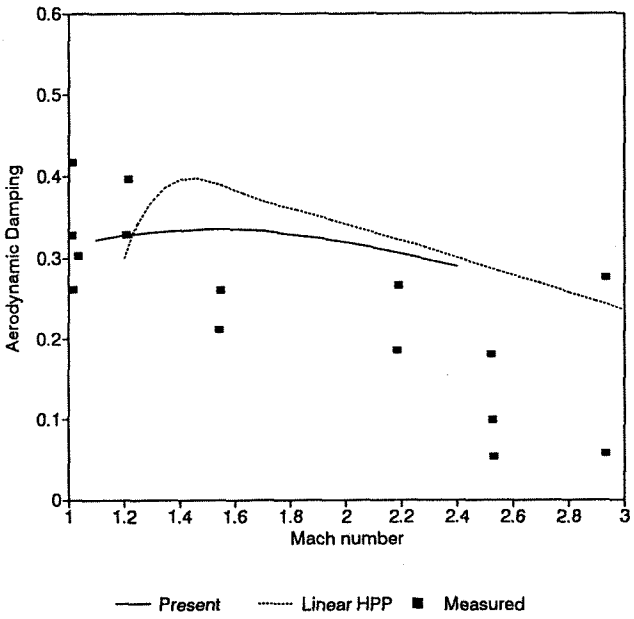

Figure 13 Aerodynamic damping coefficient of Saturn SA–1 launch vehicle first bending mode.

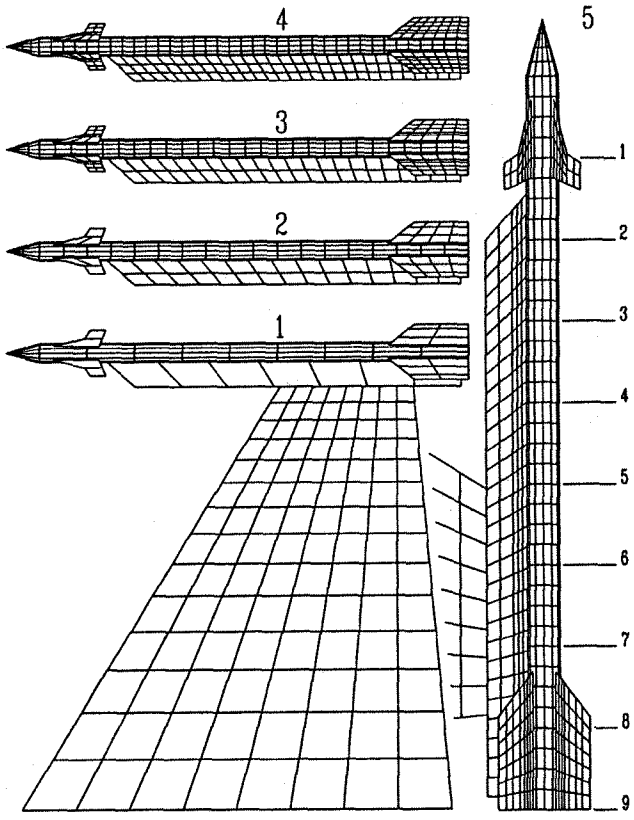

Figure 14 Different panelling schemes of F5 wing with tip missile.

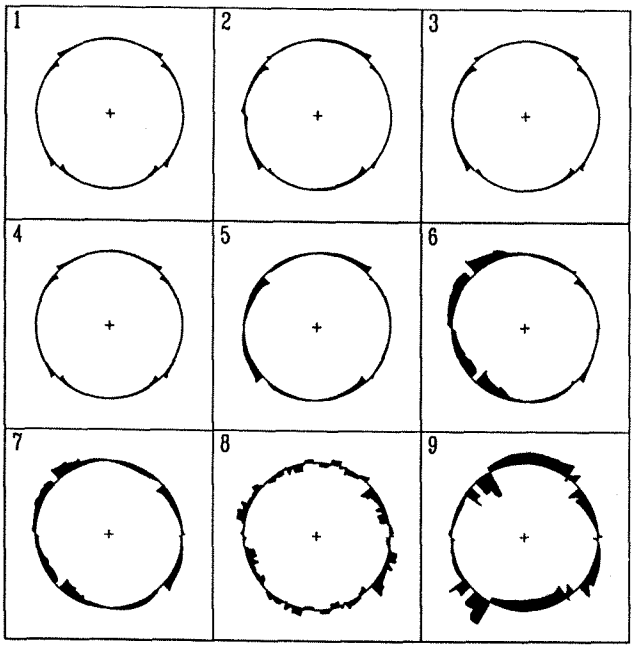

Figure 15 Residual normal velocity on missile body surface for the wing at a steady angle of attack at $M = 1.35$.

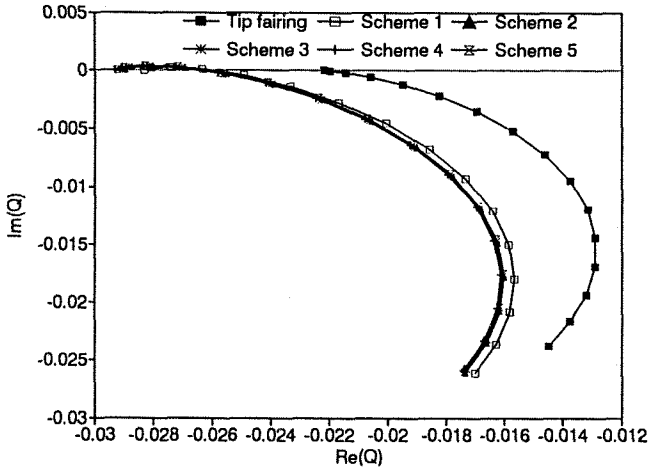

Figure 16 Generalized force Q_{11} for the F5 wing with tip missile at $M = 1.35$.

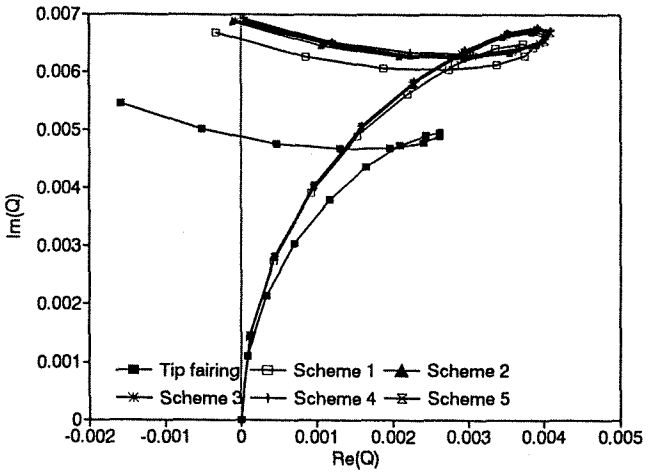

Figure 17 Generalized force Q_{12} for the F5 wing with tip missile at $M = 1.35$.

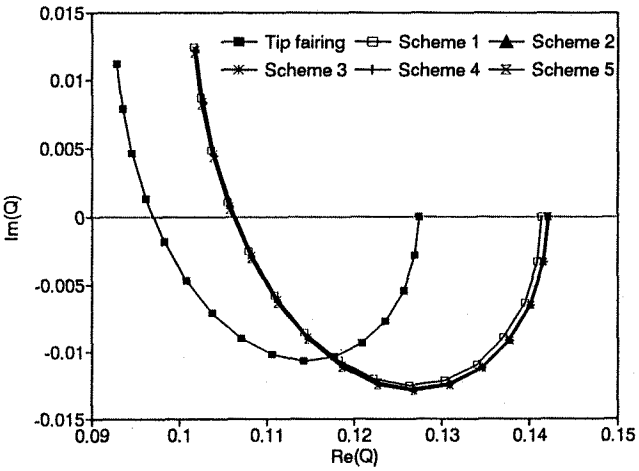

Figure 18 Generalized force Q_{21} for the F5 wing with tip missile at $M = 1.35$.

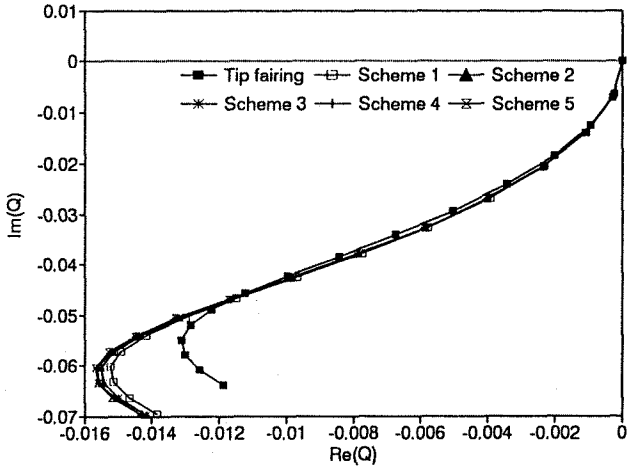

Figure 19 Generalized force Q_{22} for the F5 wing with tip missile at $M = 1.35$.

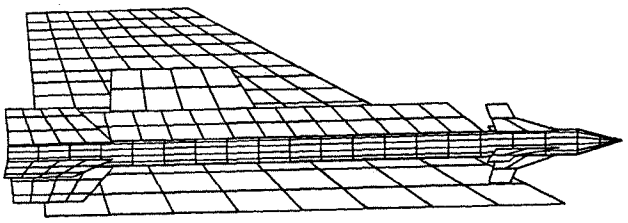

Figure 20 F5 wing with under wing store.

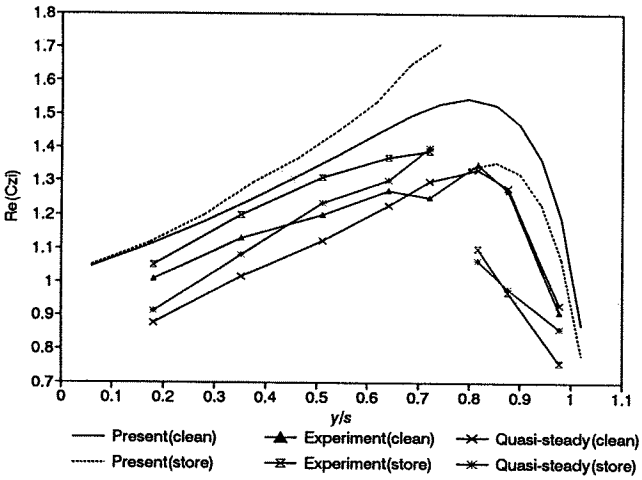

Figure 21 Comparison of calculated and measured real part of spanwise lift distribution on F5 wing with and without under wing store at $M = 1.35$ and $k = 0.1$.

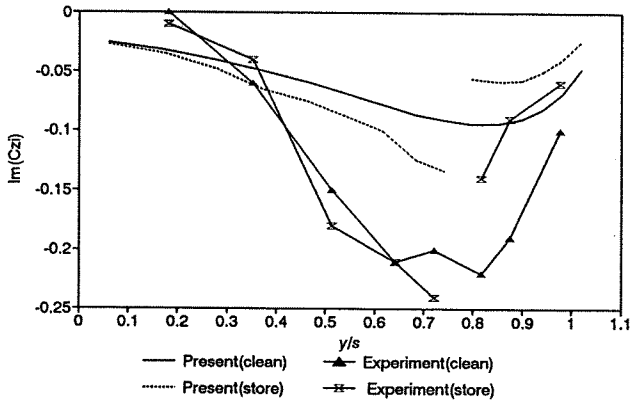

Figure 22 Comparison of calculated and measured imaginary part of spanwise lift distribution on F5 wing with and without under wing store at $M = 1.35$ and $k = 0.1$.

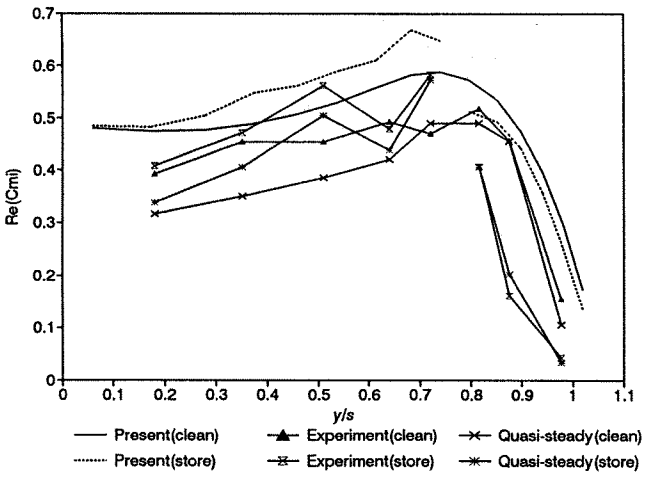

Figure 23 Comparison of calculated and measured real part of spanwise pitching moment distribution on F5 wing with and without under wing store at $M = 1.35$ and $k = 0.1$.

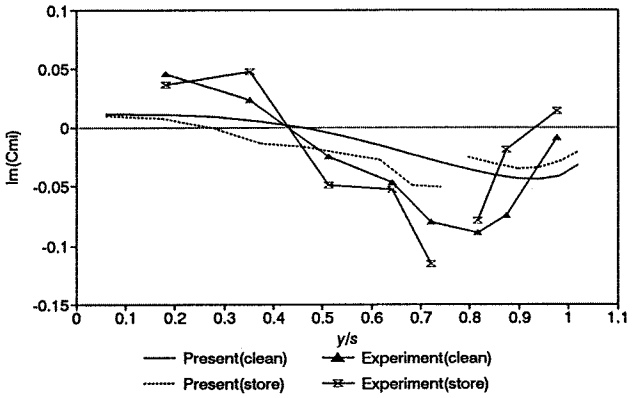

Figure 24 Comparison of calculated and measured imaginary part of spanwise pitching moment distribution on F5 wing with and without under wing store at $M = 1.35$ and $k = 0.1$.

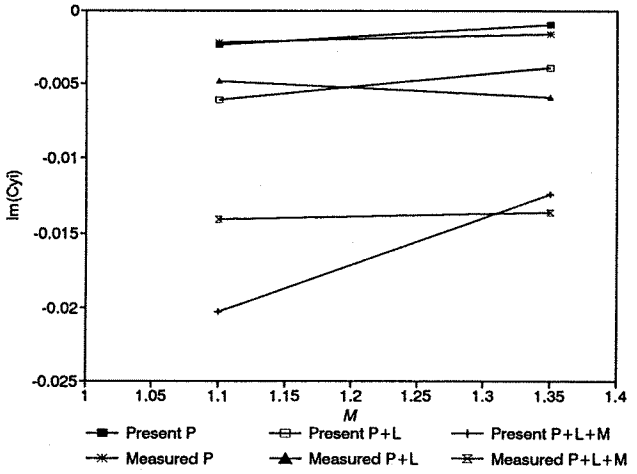

Figure 25 Comparison of calculated and measured real part of unsteady side force on under wing store in various stages of completeness at $k = 0.1$.

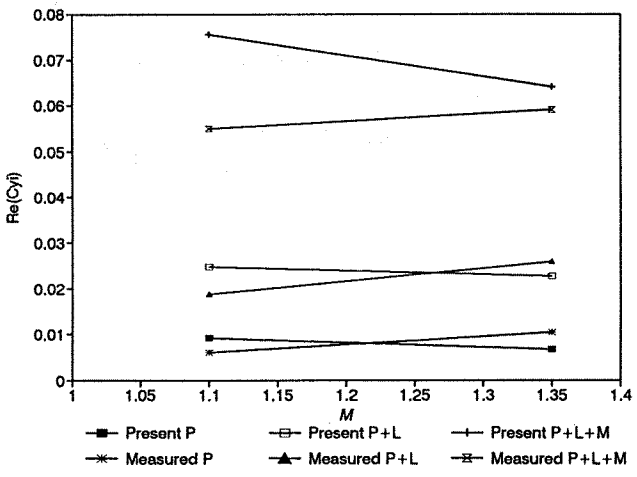

Figure 26 Comparison of calculated and measured imaginary part of unsteady side force on under wing store in various stages of completeness at $k = 0.1$.